

Monitoring the ultrafast buildup of Rabi oscillations in the time domain

Xu Zhang,¹ Yijie Liao,¹ Yongkun Chen,¹ Miao Yu,¹ Siyu Li,¹ Mingrui He,² Kunlong Liu ¹,
Peixiang Lu,^{1,3} and Yueming Zhou ^{1,*}

¹*School of Physics and Wuhan National Laboratory for Optoelectronics, Huazhong University of Science and Technology, Wuhan 430074, China*

²*Department of Basic Courses, Naval University of Engineering, Wuhan 430033, China*

³*Optics Valley Laboratory, Hubei 430074, China*



(Received 11 December 2023; revised 16 April 2024; accepted 7 May 2024; published 3 June 2024)

We theoretically study the buildup of Rabi oscillations in the two-photon ionization process in atomic Hydrogen, where both resonant and nonresonant ionization paths play a significant role. Using spectrally and angularly resolved electron interferometry, we reconstruct the temporal profiles of electron wave packets (EWPs) and the time evolution of photoelectron energy spectra (PESs) for the s and d partial waves from the numerical results of time-dependent Schrödinger equation. Our results reveal the differences between the s and d waves in terms of the minimum of the temporal EWPs and the asymmetry of the time-evolving PESs. Based on a three-level model, we attribute these phenomena to the different contributions of the nonresonant path in these two partial waves. Further, with this model we highlight the opposite effects of the AC-Stark effect on resonant and nonresonant paths. Our work directly reveals the time-varying influence of the oscillating populations on the dynamics of resonant and nonresonant paths, and provides a feasible method for assessing the partial-wave resolved contribution of the nonresonant path in the time domain.

DOI: [10.1103/PhysRevA.109.063102](https://doi.org/10.1103/PhysRevA.109.063102)

I. INTRODUCTION

Photoionization is a fundamental process in light-matter interaction, and has been extensively studied since the advent of quantum mechanics. Probing its dynamics is the central focus of attosecond science. The electronic dynamics in photoionization are completely encoded in the amplitudes and phases of electron wave packets (EWPs). Coherent attosecond light sources have enabled the application of electron interferometry techniques such as streaking [1–3], reconstruction of attosecond beating by interference of two-photon transitions (RABBIT) [4–13], and the bichromatic electric-field method [14–20]. These techniques allow for the accurate measurement of the amplitudes and phases of EWPs. By characterizing EWPs' amplitudes and phases through spectrally resolved electron interferometry, photoionization electronic dynamics is tracked in real time. Examples include the multichannel single-photoionization of rare gases [21] and the photoionization of chiral molecules [22], and so on. Notably, recent studies measured the spectral phase near Fano resonances [23,24], and successfully reconstructed the buildup of the Fano profile [25–27], thereby providing deep insights into correlated multielectron dynamics.

Using a seeded free-electron laser in the extreme-ultraviolet (XUV) frequency regime, Autler-Townes (AT) doublets [28–33] were first observed in the resonant two-photon ionization (TPI) of He recently [34]. This AT splitting is a manifestation of Rabi oscillations; the transition from

unsplit to split energy spectra indicates the buildup of Rabi oscillations [35–50]. During Rabi oscillations in TPI, electrons periodically populate the ground and resonant states. Consequently, photoionization occurs by absorbing one photon from the previously populated resonant state, or absorbing two photons from the ground state, which are referred as the resonant ionization path, and the nonresonant ionization path, respectively [34]. Recent theoretical studies [45,46] confirmed that both the resonant and nonresonant ionization path play crucial roles in the high-intensity region where Rabi oscillations occur. Their conclusions were drawn by analyzing the asymmetry of the AT doublets in the photoelectron energy spectrum. However, direct observations of the electronic dynamics for the resonant and nonresonant paths are currently lacking. Previous studies on the dynamics of EWPs of Fano resonances [23–27,51–58] have enabled the direct observation of the interference processes between the direct ionization path and the resonant ionization path (via autoionization states). In this work, we investigate the dynamics of EWPs during the buildup of Rabi oscillations. This provides deeper insights into the influence of Rabi oscillating on the dynamics of competing resonant and nonresonant ionization paths.

By numerically solving the time-dependent Schrödinger equation (TDSE), we reveal the dynamics of continuum EWPs in the resonant TPI process of hydrogen. Employing spectrally and angularly resolved electron interferometry, we separately reconstruct the temporal profiles of EWPs and time-evolving PESs for the s and d partial waves. We find that the temporal evolutions of the s and d partial waves overall are the same, such as the extrema in the temporal EWPs for

*zhouymhust@hust.edu.cn

both the s and d waves coincide with integer multiples of the Rabi period. However, notable differences are present in the details between the s and d waves in terms of the minimum of the temporal EWPs and the asymmetry of the energy spectrum. To understand these behaviors, we resort to a three-level model that includes the nonresonant ionization path and the AC-Stark effect [45]. We show that the net contribution of the nonresonant path can be deduced at the minimum of the temporal EWPs for the different partial waves. Further, our model highlights the opposite effects of the AC-Stark effect on the resonant and nonresonant paths. Additionally, we also reveal the dynamics of EWPs ionized solely from the Rabi-cycling ground state, where the extrema in the temporal EWPs coincide with half-integer multiples of the Rabi period. Our work directly reveals the influence of the oscillating populations on the electron dynamics of resonant and nonresonant paths. More importantly, we provide a feasible method for quantitatively assessing the partial-wave resolved contribution of the nonresonant path in the time domain.

This paper is structured as follows. In Sec. II, we describe the methods of numerically solving the three-dimensional-TDSE (3D-TDSE). Section III A shows the reconstructed temporal EWPs in the resonant TPI, and the analysis of temporal EWPs using the three-level model is shown in Sec. III B. In Sec. III C, we reconstruct and analyze the temporal evolution of the EWPs from the Rabi-cycling ground state. Section IV summarizes our work. Appendix A provides details on the three-level model, Appendix B presents a comparison between the model and TDSE results, and Appendix C provides a detailed explanation of the role of all laser pulses introduced in our work.

II. METHODS

To monitor the buildup of Rabi oscillations in the TPI process of hydrogen, the photoelectron momentum distributions (PEMDs) are obtained by numerically solving the 3D-TDSE [59] of the hydrogen atomic system in the velocity gauge.

The TDSE is expressed [in atomic units (a.u.)] as

$$i \frac{\partial \psi(\mathbf{r}, t)}{\partial t} = H(\mathbf{r}, t) \psi(\mathbf{r}, t), \quad (1)$$

where

$$H(\mathbf{r}, t) = -\frac{1}{2} \nabla^2 - \frac{1}{r} - i \mathbf{A}_\omega(t) \cdot \nabla. \quad (2)$$

$\mathbf{A}_\omega(t) = A_0 \sin^2(\frac{\pi t}{\tau}) \sin(\omega t) \mathbf{e}_z$ is the vector potential of the laser pulse, linearly polarized along the z axis. A_0 is the amplitude of the vector potential, ω is the angular frequency of the laser pulse, and τ is the finite pulse duration of the laser pulse.

The wave function of the TDSE in Eq. (1) is expanded using the spherical harmonics $Y_{l,m}$, $\psi(\mathbf{r}, t) = \sum_{l,m} \frac{R_{lm}(r,t)}{r} Y_{l,m}$, where l and m represent the angular momentum quantum number and the magnetic quantum number, respectively. $R_{lm}(r, t)$ is the radial part of the wave function, and is discretized by the finite-element discrete variable representation method [60]. The time propagation of the TDSE is calculated by the split-Lanczos method [61]. In each step of the propagation, we split the wave function $\psi(\mathbf{r}, t)$ into the inner part $\psi_{in}(\mathbf{r}, t) = \psi(\mathbf{r}, t) F_{ab}$, and outer part $\psi_{out}(\mathbf{r}, t) = \psi(\mathbf{r}, t) (1 - F_{ab})$, where $F_{ab} = 1 - (1 + e^{(R-R_c)/d})^{-1}$ is the absorbing mask function. The inner part $\psi_{in}(\mathbf{r}, t)$ evolves according to Eq. (1), and $\psi_{out}(\mathbf{r}, t)$ is propagated by the

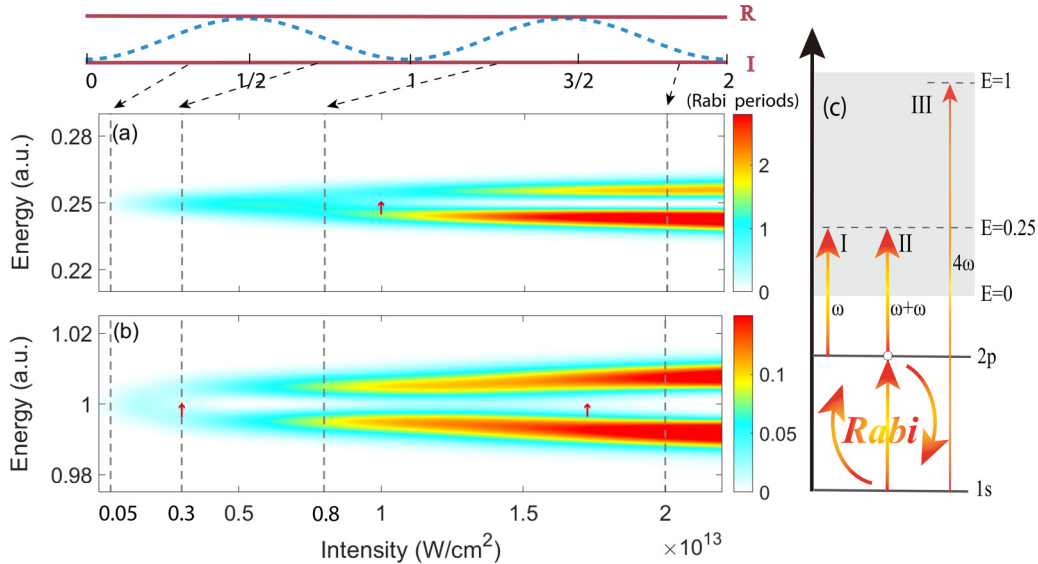


FIG. 1. (a) PESs for the resonant TPI of hydrogen as a function of laser intensity. The laser frequency is $\omega = 0.375$ a.u., which is resonant with the $1s$ - $2p$ transition in atomic hydrogen. The dashed gray lines mark laser intensities of 5×10^{11} , 3×10^{12} , 8×10^{12} , and 2×10^{13} W/cm², corresponding to the intensities where the atom undergoes four different 1/2 Rabi periods during the laser pulses. (b) PESs ionized from the ground state of the Rabi-cycling atom by the 4ω laser pulse. The Rabi oscillation of the atom is driven by the field ω . The horizontal axis indicates the laser intensity of this dressing field (ω). The red arrows in (a) and (b) indicate the splitting of the energy spectra. (c) Schematic diagrams of the ionization paths involved in (a) and (b). I and II represent the resonant and nonresonant ionization paths, respectively, in the TPI process in (a). III represents the ionization path from the Rabi-cycling ground state induced by the weak 4ω laser in (b).

Coulomb-Volkov propagator [62]. The ionization amplitude is extracted by projecting the final wave function to the scattering states. In our simulation, the maximum of angular momentum quantum number is $L_{\max} = 30$, and the magnetic quantum number is set to $m_{\max} = 0$ because of the linear polarization of the laser fields in our calculations. The time step is fixed at $\Delta t = 0.01$ a.u.. The maximal box size for the radial coordinate R_{\max} is chosen to be 1000 a.u.. The radius of the mask function R_c is 800 a.u., $d = 2$ a.u. The convergence of our calculations is confirmed by changing these parameters.

III. NUMERICAL RESULTS AND DISCUSSIONS

We calculate the photoelectron energy spectra of the resonant TPI during the buildup of Rabi oscillations. The laser frequency is $\omega = 0.375$ a.u., which is resonant with the $1s$ - $2p$ transition in atomic hydrogen. The pulse duration is $\tau = 1340$ a.u. (full width as half maximum, FWHM $\cong 16$ fs, spectral bandwidth $\cong 0.009$ a.u.). The energy spectra as a function of laser intensity are displayed in Fig. 1(a). In the low-intensity region, the energy spectra exhibit a single peak located at 0.25 a.u.. The AT doublets are clearly observed in the energy spectra beyond the intensity of 1×10^{13} W/cm² [as indicated by the red arrow in Fig. 1(a)], and the energy spacing between the doublets gradually increases with increasing laser intensity. This splitting is a manifestation of Rabi oscillations, and the transition from unsplit to split energy spectra represents the buildup of Rabi oscillations [35–41,43–48]. The heights of the doublets are obviously asymmetric, with the height of the lower-energy peak being higher. This asymmetry is attributed to the combined effects of the AC-Stark shift, and interference of the resonant and nonresonant ionization paths [34,45,46]. Because both the resonant [path I in Fig. 1(c)] and the nonresonant path (path II) contribute in this laser intensity region [34,45], we introduce a weak 4ω laser field to induce photoionization of the Rabi-cycling atom from the ground state [path III in Fig. 1(c)]. With this method, the dynamics of the ground state, and thus the nonresonant ionization path can be isolated and revealed (see Appendix C for a detailed discussion on the role of the 4ω laser field). The energy spectra due to the 4ω laser as a function the intensity of ω field are shown in Fig. 1(b). Compared with Fig. 1(a), the splitting of the energy spectra occurs at a significantly lower intensity [approximately 0.3×10^{13} W/cm², indicated by the first arrow in Fig. 1(b)]. More intriguingly, after splitting, the photoelectron population between AT doublets increases with increasing laser intensity, followed by a subsequent decrease. The splitting of the energy spectra occurs twice within the first two Rabi periods [as indicated by the two red arrows in Fig. 1(b)].

To reveal the buildup of Rabi oscillations in real-time, we use spectrally and angularly resolved electron interferometry to measure the phase of photoelectrons, and then reconstruct the continuum EWP dynamics. This reconstruction method was initially introduced in [26] for monitoring Fano resonance. Here, we reconstruct the continuum EWP dynamics in the resonant TPI [i.e., EWPs from paths I and II in Fig. 1(c)], as discussed in Sec. III A, and subsequently analyzed in Sec. III B with the three-level model [45]. Furthermore, the dynamics of EWPs originating solely from the Rabi-cycling

ground state [i.e., EWPs from path III in Fig. 1(c)] are reconstructed and analyzed in Sec. III C.

A. Reconstruction of the temporal evolution of EWPs in resonant TPI from TDSE data

To monitor the continuum EWP dynamics in the resonant TPI during the buildup of Rabi oscillations, we employ a

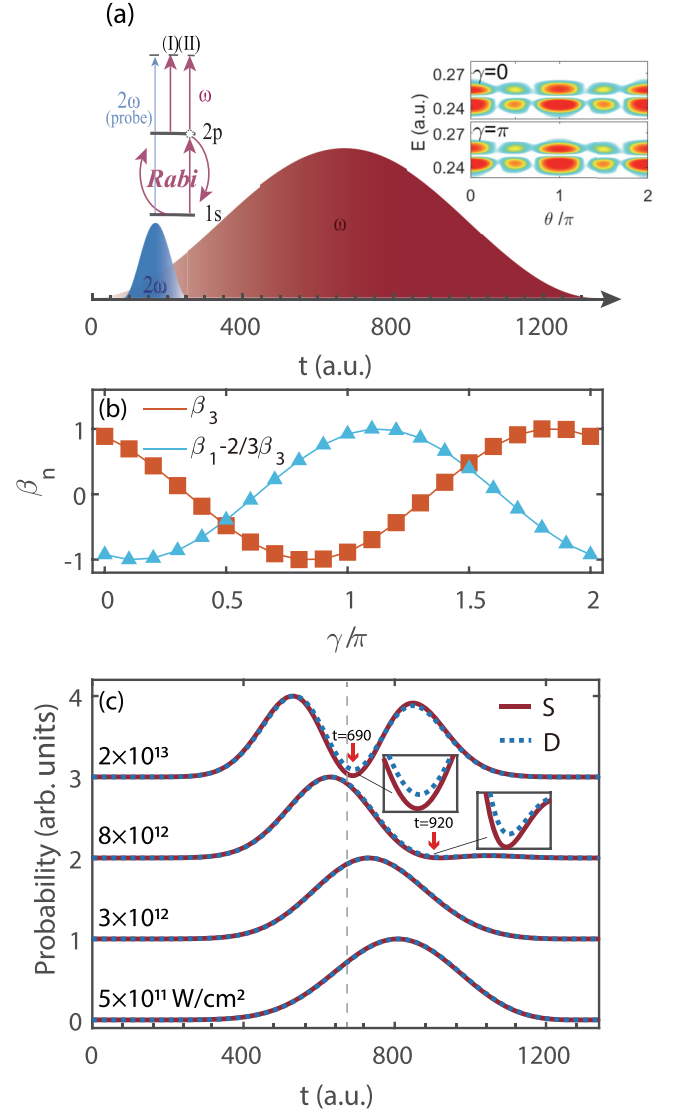


FIG. 2. (a) Schematic diagrams of the laser pulses used to probe EWP dynamics in the resonant TPI. The ω pulse (red) induces the resonant TPI of hydrogen. A weak 2ω laser pulse (blue) is introduced at the leading edge of the resonant ω pulse. The EWPs ionized by the 2ω pulse (indicated by blue arrow) serve as a reference for probing the EWPs ionized by the ω pulse (indicated by red arrows). Inset: PEMDs at the laser intensity of 2×10^{13} W/cm². (b) Normalized β_3 (red squares) and $\beta_1 - \frac{2}{3}\beta_3$ (blue triangles) as functions of the phase γ at the laser intensity of 2×10^{13} W/cm². (c) Normalized probability of the temporal profiles of EWPs $|\tilde{A}_s(t)|^2$ (solid red lines) and $|\tilde{A}_d(t)|^2$ (dashed blue lines) for the s and d waves at laser intensities of 5×10^{11} , 3×10^{12} , 8×10^{12} , and 2×10^{13} W/cm². As visual aids, the lines in (c) have been vertically separated and the differences between s - and d -waves are scaled up in the insets.

weak 2ω pulse at the leading edge of the resonant ω pulse, as illustrated in Fig. 2(a) (see Appendix C for a detailed discussion on the role of the 2ω pulse). The carrier-envelope phase (CEP) of the ω pulse remains fixed, whereas the CEP of the 2ω pulse, denoted by γ , varies from 0 to 2π . The EWPs ionized by the 2ω pulse serve as the reference for probing the amplitudes and phases of the EWPs ionized by the ω pulse [as shown in Fig. 2(a)]. In contrast to the conventional bichromatic field method [14–20], the probe 2ω pulse in our

scheme is shortened and located before the ω pulse, to avoid extra phase due to the oscillating populations of the ground state. The specific delay between the 2ω and ω pulses does not affect the phase measurement. The interference of the EWPs ionized by the ω and 2ω pulses determines the PEMDs, which depend on the relative phase γ between these two pulses, as shown in the inset of Fig. 2(a). The phase (γ) dependence of the PEMDs can be expressed using the partial coherence method [63]

$$\begin{aligned} I(\theta) &= ||A_s|e^{i(\phi_s - \frac{\pi}{2})}Y_{00}(\theta, \varphi) + |A_d|e^{i(\phi_d - \frac{3\pi}{2})}Y_{20}(\theta, \varphi) + |A_p|e^{i(\phi_p - \pi - \gamma)}Y_{10}(\theta, \varphi)|^2 \\ &= \beta_0 P_0(\theta) + \beta_1 P_1(\theta) + \beta_2 P_2(\theta) + \beta_3 P_3(\theta) + \beta_4 P_4(\theta), \end{aligned} \quad (3)$$

where $A_{s,p,d}$ are the amplitudes of the partial waves, $\phi_{s,p,d}$ represent the corresponding phases, and θ is the polar angle of the photoelectron with respect to the polarization direction of the laser fields. Here the p partial wave results from the single-photon ionization by the 2ω field, while the s and d partial waves are from the two-photon ionization by the ω field. The asymmetry parameters β_n are determined as functions of A_p , A_s , and A_d as follows:

$$\begin{aligned} \beta_0 &= \frac{1}{4\pi} (|A_p|^2 + |A_s|^2 + |A_d|^2) \\ \beta_1 &= \frac{1}{4\pi} \left[\frac{4}{5} \sqrt{15} |A_d| |A_p| \cos \left(\gamma + \left(\phi_d - \phi_p - \frac{\pi}{2} \right) \right) \right. \\ &\quad \left. + 2\sqrt{3} |A_p| |A_s| \cos \left(\gamma + \left(\phi_s - \phi_p + \frac{\pi}{2} \right) \right) \right] \\ \beta_2 &= \frac{1}{4\pi} \cdot \frac{1}{7} \left[\frac{10|A_d|^2 + 14|A_p|^2}{+14\sqrt{5}|A_d||A_s| \cos(\phi_d - \phi_s - \pi)} \right] \\ \beta_3 &= \frac{1}{4\pi} \cdot \frac{6}{5} \sqrt{15} |A_d| |A_p| \cos \left[\gamma + \left(\phi_d - \phi_p - \frac{\pi}{2} \right) \right] \\ \beta_4 &= \frac{1}{4\pi} \cdot \frac{18}{7} |A_d|^2 \\ \left(\beta_1 - \frac{2}{3} \beta_3 \right) &= \frac{1}{4\pi} \cdot 2\sqrt{3} |A_p| |A_s| \cos \left[\gamma + \left(\phi_s - \phi_p + \frac{\pi}{2} \right) \right]. \end{aligned} \quad (4)$$

β_3 and $(\beta_1 - \frac{2}{3}\beta_3)$ oscillate with the phases γ , as shown in Fig. 2(b). We employ β_3 and $(\beta_1 - \frac{2}{3}\beta_3)$ to determine the phases of the s and d partial waves, and use the maximum values of β_3 , β_4 , and $(\beta_1 - \frac{2}{3}\beta_3)$ to determine their amplitudes. Repeating the above procedure, the amplitudes and phases at different energies within the energy range 0.21–0.28 a.u. are retrieved, then the dynamics of TPI in Fig. 1(a) [i.e., the paths I and II in Fig. 1(c)] can be revealed in the time domain. We mention that our procedure is applicable to the experimental data if the photoelectron momentum distributions from the two-color field are measured.

Using the Fourier transform, the temporal profiles of the EWPs are reconstructed from the retrieved phases $\phi_{s(d)}(E)$ and amplitudes $A_{s(d)}(E)$ [26],

$$\tilde{A}_{s(d)}(t) = \frac{1}{2\pi} \int_{-\infty}^{\infty} |A_{s(d)}(E)| e^{i\phi_{s(d)}(E)} e^{-iEt} dE. \quad (5)$$

Figure 2(c) shows the probability of the temporal EWPs (i.e., ionization rate [51]) $|\tilde{A}_{s(d)}(t)|^2$ for the s and d waves at four laser intensities, 5×10^{11} , 3×10^{12} , 8×10^{12} , and

2×10^{13} W/cm². At these four different intensities, the atom undergoes nearly 1/2, 1, 3/2, and 2 Rabi periods, respectively, during the laser pulse. At low intensities of 5×10^{11} and 3×10^{12} W/cm², the temporal EWPs display a single-peak structure. The peak of the temporal EWP lags behind the peak of the laser pulse [indicated by dashed gray line in Fig. 2(c)], and the time delay between them is laser intensity dependent. This phenomenon is different from the perturbation case, where the peak of the temporal EWP coincides with that of the laser pulse. As the laser intensity increases, the temporal profiles of the s and d waves evolve from a single-peak structure to a double-peak structure, with a trough located at $t = 920$ a.u. at the intensity of 8×10^{12} W/cm² and shifted to $t = 690$ a.u. at 2×10^{13} W/cm². The occurrence of these troughs is approximately synchronous with the completion of one Rabi period (i.e., the instants $t = 920$ a.u. and 690 a.u. roughly correspond to one Rabi period at the intensity of 8×10^{12} W/cm² and 2×10^{13} W/cm², respectively.). Furthermore, at low intensities, the (normalized) probability of the temporal EWPs for the s and d waves are nearly identical. However, in the higher intensity region, differences emerge

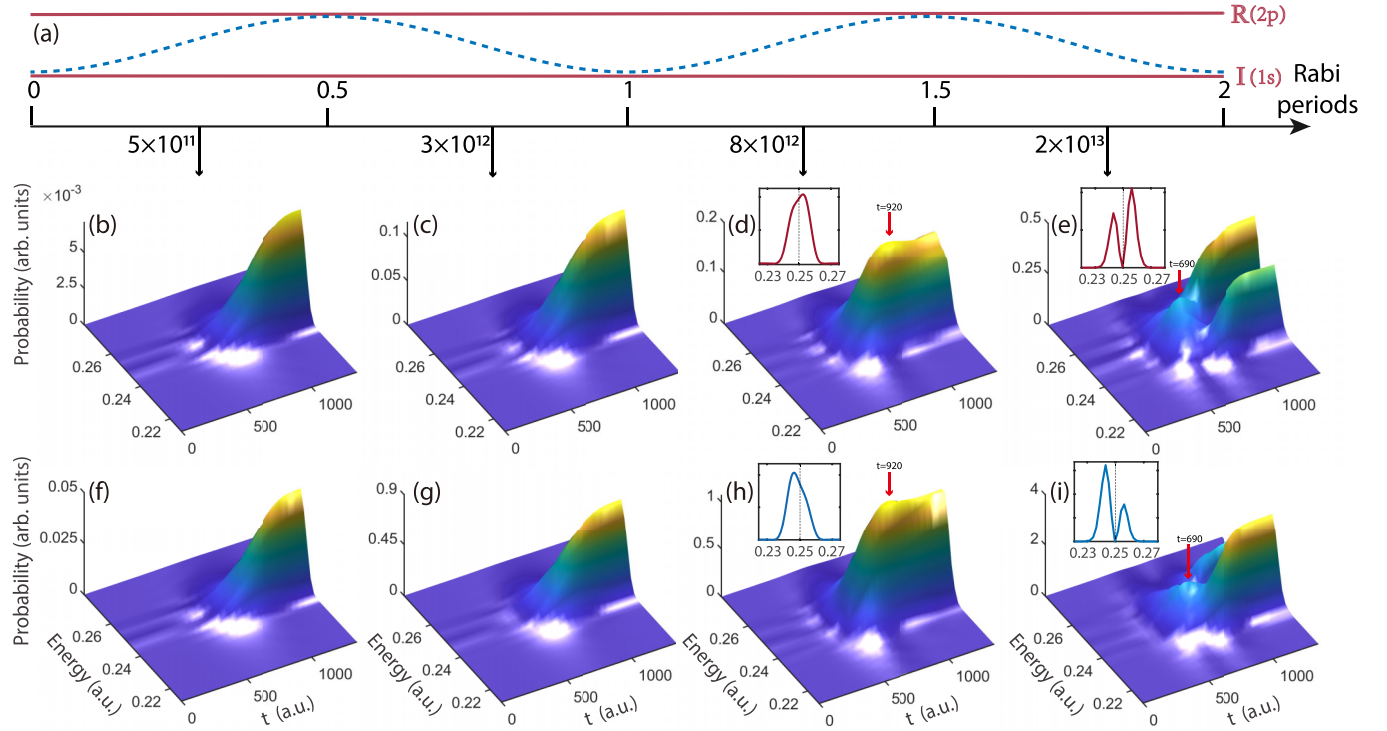


FIG. 3. (a) Schematic representation of the first two Rabi periods. The dashed blue line indicates the population transfer between the ground (I) and the resonant (R) states as a function of the Rabi periods (calculated with the three-level model [45]). The arrows below the time axis indicate the laser intensities corresponding to four different $1/2$ Rabi period intervals. [(b)–(i)] Time evolution of the photoelectron energy spectrum in the resonant TPI at laser intensities of 5×10^{11} , 3×10^{12} , 8×10^{12} , and 2×10^{13} W/cm², for the [(b)–(e)] s -wave and [(f)–(i)] d -wave. The insets in (d), (h) and (e), (i) show the energy spectrum at the end of accumulation time.

at the minimum values of the temporal profiles of EWPs. We will explain all of these features with the three-level model [45] in the subsequent subsection.

Using the temporal wave packets of Eq. (5), the time evolution of the photoelectron energy spectrum $P_{s(d)}(E, t)$ for the s and d waves can be reconstructed by the limited inverse Fourier transform [26]

$$P_{s(d)}(E, t) = \left| \int_{-\infty}^t \tilde{A}_{s(d)}(t') e^{iEt'} dt' \right|^2. \quad (6)$$

Figures 3(b) to 3(e) and 3(f) to 3(i) depict the time evolution of the photoelectron energy spectrum for the s wave and d wave, respectively. As the laser intensity increases, the evolution of $P_{s(d)}(E, t)$ exhibits a single-peak structure until it reaches its maximum, followed by a decrease and eventually splitting into a double structure. The instants at which $P_s(E, t)$ and $P_d(E, t)$ reach their extreme values [indicated by the red arrows in Figs. 3(b) to 3(i)] roughly coincide with the completion of one Rabi period. This can be understood from Eq. (6), which implies that the extreme value of $P_{s(d)}$ is located at the minimum value of $\tilde{A}_{s(d)}$. However, Figs. 3(d) and 3(h) and 3(e) and 3(i) show that the asymmetry in the time-evolving energy spectra differs between s and d waves at high laser intensities. For the s wave, more photoelectrons are distributed in energy regions above 0.25 a.u., whereas the d wave exhibits the opposite trend.

B. Analysis of temporal evolution of EWPs in resonant TPI by the three-level model

1. Temporal evolution of EWPs derived from the three-level model

To understand the temporal evolution of the EWPs in resonant TPI shown in Figs. 2 and 3, we resort to a three level-model [45] (see Appendix A). The temporal evolutions of the EWPs from this model are in excellent agreement with the results from the TDSE (see Appendix B). Based on this three level-model, the time-dependent amplitude of the continuum state can be written as

$$i\dot{\tilde{a}}_\varepsilon(t) = \tilde{M}_{I\varepsilon}^\dagger \left(\frac{1}{2} E_0 g(t) \right)^2 e^{-i\tilde{\delta}_I t} \tilde{a}_I(t) + \tilde{D}_{R\varepsilon}^\dagger \cdot \frac{1}{2} E_0 g(t) \cdot e^{-i\tilde{\delta}_R t} \tilde{a}_R(t), \quad (7)$$

where $|I\rangle$, $|R\rangle$, and $|\varepsilon\rangle$ represent the ground ($1s$), resonant ($2p$), and continuum states, respectively. $\tilde{M}_{I\varepsilon}^\dagger$ is the two-photon transition matrix element from the ground state to the continuum state via the nonresonant intermediate states (i.e., including all the bound and continuum intermediate states except the resonant $2p$ state), and $\tilde{D}_{R\varepsilon}^\dagger$ is the transition dipole matrix element between the resonant and continuum states. The terms $\tilde{\delta} = E_R + S_R - E_\varepsilon - S_\varepsilon + \omega$ and $\tilde{\delta}_I = E_I + S_I - E_\varepsilon - S_\varepsilon + 2\omega$ denote the energy detunings, and S_i ($i = I, R, \varepsilon$) is the AC-Stark shift. $\tilde{a}_I(t)$ and $\tilde{a}_R(t)$ represent the amplitudes of the ground and resonant states, respectively. By performing Fourier transform on \tilde{a}_ε , we can derive the expression of the

temporal amplitude $\tilde{a}(t)$ as

$$\begin{aligned}\tilde{a}(t) &= \frac{1}{2\pi} \int_{-\infty}^{\infty} \tilde{a}_\varepsilon(E) e^{-iEt} dE \\ &= \tilde{M}_{I\varepsilon}^\dagger \left(\frac{1}{2} E_0 g(t) \right)^2 e^{-i(E_I + S_I - S_\varepsilon + 2\omega)t} \tilde{a}_I(t) \\ &\quad + \tilde{D}_{R\varepsilon}^\dagger \frac{1}{2} E_0 g(t) e^{-i(E_R + S_R - S_\varepsilon + \omega)t} \tilde{a}_R(t).\end{aligned}\quad (8)$$

The temporal EWP obtained via Fourier transform from TDSE data [Eq. (5)] is equivalent to the temporal amplitude $\tilde{a}(t)$ derived from the three-level model. This equivalence has been theoretically confirmed [51], and further validated in this study (for the Rabi-cycling system) by the excellent agreement between the numerical results of $\tilde{A}(t)$ from TDSE and $\tilde{a}(t)$ from the three-level model (Fig. 8). $|\tilde{a}(t)|^2$ represents the ionization rate; thus, the probability of the temporal EWP from the TDSE data $|\tilde{A}(t)|^2$ is physically meaningful as the ionization rate [51].

Based on the equivalence between $\tilde{A}(t)$ and $\tilde{a}(t)$, we then express the temporal EWP as the sum of two components

$$\begin{aligned}\tilde{A}(t) &= \tilde{M}_{I\varepsilon}^\dagger \left(\frac{1}{2} E_0 g(t) \right)^2 e^{-i(E_I + S_I - S_\varepsilon + 2\omega)t} \tilde{a}_I(t) \\ &\quad + \tilde{D}_{R\varepsilon}^\dagger \frac{1}{2} E_0 g(t) e^{-i(E_R + S_R - S_\varepsilon + \omega)t} \tilde{a}_R(t),\end{aligned}\quad (9)$$

where the first component corresponds to EWPs from the nonresonant ionization path, and the second component corresponds to EWPs from the resonant ionization path. $\tilde{a}_I(t)$ [$\sim \cos(\frac{1}{2}\Omega t)$] and $\tilde{a}_R(t)$ [$\sim \sin(\frac{1}{2}\Omega t)$] represent the real-valued amplitudes of the ground and resonant states, respectively, which oscillate periodically with the effective Rabi frequency Ω . Equation (9) indicates that the temporal evolution of the EWP is affected by the oscillating amplitudes of the atomic states $\tilde{a}_{I,R}(t)$. This differs from the perturbative case in which the temporal EWP follows the pulse envelope $g(t)$. Consequently, as shown in Fig. 2(c), the peak of the probability of the temporal EWPs (ionization rate) lags behind that of the laser pulse. The amplitudes $\tilde{a}_{I,R}(t)$ depend on laser intensity, thus resulting in variations in the temporal EWPs with increasing laser intensity.

With Eq. (9), the time-evolving photoelectron energy spectrum, which is the limited inverse Fourier transform of $\tilde{A}(t)$, can be expressed as

$$\begin{aligned}P(E, t) &= \left| \int_{-\infty}^t \tilde{A}(t') e^{iEt'} dt' \right|^2 \\ &= \left| \int_{-\infty}^t \tilde{M}_{I\varepsilon}^\dagger \left(\frac{1}{2} E_0 g(t') \right)^2 e^{-i\delta_I t'} \tilde{a}_I(t') \right. \\ &\quad \left. + \tilde{D}_{R\varepsilon}^\dagger \frac{1}{2} E_0 g(t') e^{-i\delta_R t'} \tilde{a}_R(t') dt' \right|^2.\end{aligned}\quad (10)$$

Equations (9) and (10) indicate that the temporal evolution of the EWPs are determined by the combined effects of

oscillating amplitudes of the ground and resonant states, and the competition between resonant and nonresonant ionization paths. In the intensity range in our calculations, the contribution of the resonant path is much larger than the nonresonant path [34,45]. So, we first analyze the contribution of the resonant path [i.e., the second term in Eqs. (9) and (10)].

2. Contribution of the resonant path to temporal evolution of EWPs

At laser intensities below 3×10^{12} W/cm², the atom undergoes less than one Rabi period in the laser pulse [Fig. 3(a)], during which $\tilde{a}_R(t)$ [$\sim \sin(\frac{1}{2}\Omega t)$] remains positive. Consequently, $|\tilde{A}(t)|$ (or $|\tilde{A}(t)|^2$), mainly influenced by the resonant path [the second term in Eq. (9)], exhibits a single-peak structure, as shown in Fig. 2(c), and $P(E, t)$ [Eq. (10)] continues to increase, as shown in Fig. 3. As the laser intensity increases to 8×10^{12} W/cm², the atom undergoes more than one Rabi period. At approximately $t = 920$ a.u., the atom completes one Rabi oscillation and then $\tilde{a}_R(t)$ becomes negative. The change of $\tilde{a}_R(t)$ from positive to negative values leads to the occurrence of the minimum in $|\tilde{A}(t)|$ (or $|\tilde{A}(t)|^2$), and correspondingly the extrema in $P(E, t)$ at this instant. As the laser intensity further increases to 2×10^{13} W/cm², the atom undergoes nearly two Rabi periods. The atom completes one Rabi period at $t = 690$ a.u., where $\tilde{a}_R(t)$ approaches zero, thereby resulting in the occurrence of a minimum in $|\tilde{A}(t)|$ (or $|\tilde{A}(t)|^2$) and an extrema in $P(E, t)$ at this instant. After that, the atom undergoes the second Rabi period during the following part of the pulse, and thus the value of $\tilde{a}_R(t)$ becomes negative. The electron signals during the first and the second Rabi periods almost cancel each other, resulting in the complete splitting of the energy spectrum, as shown in Figs. 3(e) and 3(i).

In the resonant path, the temporal evolution of the EWPs is determined by the product of the pulse envelope $g(t)$ and $\tilde{a}_R(t)$, as indicated by the second term in Eqs. (9) and (10). This product is the same for the s and d waves. Therefore, the (normalized) probability of temporal EWPs (ionization rate) and time-evolving energy spectrum for the s and d waves are overall the same, as shown in Figs. 2(c) and 3(b) to 3(i).

3. Contribution of the nonresonant path to temporal evolution of EWPs

The minor difference between the s and d waves originates from the contribution of the nonresonant path. In Figs. 4(a) and 4(b), we present the amplitude of the temporal profiles for the s and d waves $|\tilde{A}_{s/d}(t)|$ at laser intensities of 8×10^{12} W/cm² and 2×10^{13} W/cm², respectively. The sums of these two waves $|\tilde{A}_{\text{tot}}(t)|$ ($|\tilde{A}_{\text{tot}}(t)| = |\tilde{A}_s(t) + \tilde{A}_d(t)|$) are represented by the solid lines in Fig. 4(c). The corresponding time-evolving energy spectrum at the intensity of 2×10^{13} W/cm² is shown in Figs. 4(d) to 4(f). As shown in Figs. 4(a) to 4(c), the values of the minima in temporal profiles deviate from zero, and these values increase with increasing laser intensity. For the resonant path, this value will be zero because the amplitude of the resonant state $\tilde{a}_R(t)$ is zero, which occurs at the integer Rabi period. Thus, the nonzero value of the minimum is an indication of the contribution of the nonresonant path. To address this issue, we exclude

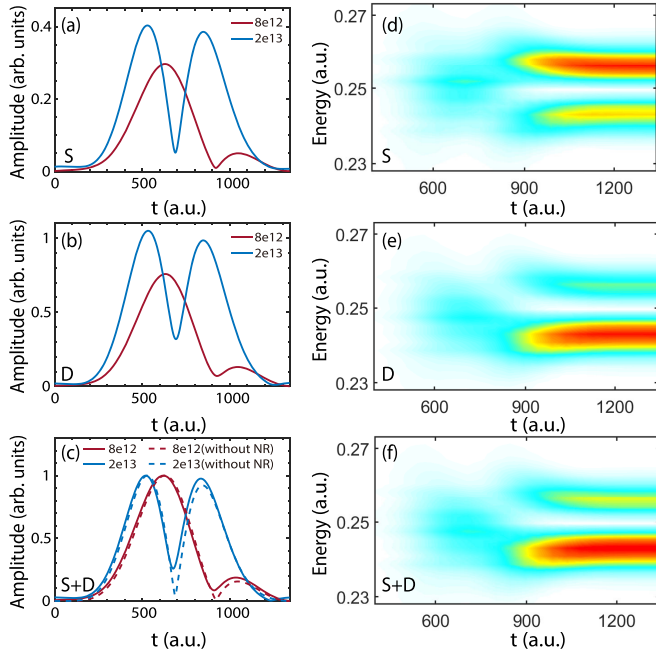


FIG. 4. (a) Amplitude of the temporal profiles of the s -wave packets $|\tilde{A}_s(t)|/4\pi$ at laser intensities of 8×10^{12} W/cm² (red solid line) and 2×10^{13} W/cm² (blue solid line). (b) Amplitude of the temporal profiles of the d -wave packets $|\tilde{A}_d(t)|/4\pi$. (c) Amplitude of the temporal profiles of the total wave packet $|\tilde{A}_{\text{tot}}(t)|/4\pi$ ($\tilde{A}_{\text{tot}}(t) = |\tilde{A}_s(t) + \tilde{A}_d(t)|$) (solid lines). For comparison, the results without considering the nonresonant path are plotted with dashed lines. (d) Time evolution of the photoelectron energy spectrum for the s wave. (e) Time evolution of the photoelectron energy spectrum for the d wave. (f) Time evolution of the total ($s + d$) photoelectron energy spectrum. The laser intensities in [(d)–(f)] are 2×10^{13} W/cm².

the nonresonant path in the three-level model [45], and the obtained temporal profiles of EWPs for the sum of the s and d waves are shown as the dashed lines in Fig. 4(c). It is shown that the minimum values reach zero when the nonresonant ionization path is excluded. As the laser intensity increases, the contribution of the nonresonant path increases, causing the value of the minimum to increase, as shown in Figs. 4(a) to 4(c). Therefore, the value of the minimum provides a way to quantitatively assess the contribution of the nonresonant path in the time domain.

For the s and d waves, the relative contribution of the nonresonant and resonant paths differs due to the different values of $\tilde{M}_{I_e}^\dagger/\tilde{D}_{R_e}^\dagger$ for the s and d partial waves. Therefore, the values for the minimum of the temporal profiles for the s and d waves are different as shown in Figs. 4(a) and 4(b), with the d wave being larger. This indicates the larger contribution of the nonresonant path in the d wave.

4. Asymmetry in time-evolving energy spectrum contributed by the resonant and nonresonant paths

To gain further insights into the asymmetry of the time-evolving energy spectrum, in Fig. 5, we show the results calculated by the three-level model [45] at the intensity of 2×10^{13} W/cm². Figure 5(a) shows the time evolution of the total photoelectron energy spectrum (the coherent summation

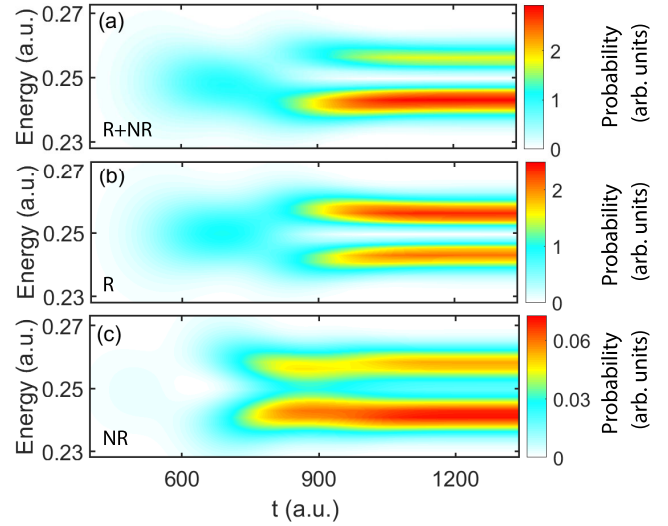


FIG. 5. Time-evolution of the total ($s + d$) photoelectron energy spectrum calculated by the three-level model when considering (a) both resonant and nonresonant ionization paths, (b) only the resonant ionization path, and (c) only the nonresonant ionization path. The laser intensity is 2×10^{13} W/cm².

of the resonant and nonresonant paths). It is in good agreement with the TDSE results shown in Fig. 4(f). Figures 5(b) and 5(c) separately show the time evolution of the photoelectron energy spectrum from the resonant and nonresonant paths, respectively. When the spectra are separated for the resonant and the nonresonant paths, they are also asymmetric. This asymmetry results from the AC-Stark shifts of the atomic states. The AC-Stark shifts have opposite signs for the ground and resonant states [45,46]. Consequently, the AC-Stark effect has opposite impacts on the asymmetry of the AT doublets for the resonant ionization path (from the resonant state) and the nonresonant ionization path (from the ground state). In the resonant (nonresonant) paths, the population at the higher (lower) energy peak is larger.

For the s and d waves, the contributions of the nonresonant path are different, as shown in Figs. 4(a) and 4(b). So, when the resonant and nonresonant paths are coherently summed, the corresponding energy spectra for the s and d waves are different, as shown in Figs. 4(d) and 4(e).

C. Reconstruction of the temporal evolution of EWPs ionized from the Rabi-Cycling ground state

In Secs. III A and B, we monitored and analyzed the dynamics of EWPs in the TPI during the buildup of the Rabi oscillations. During this process, both the resonant path (from the resonant state) and nonresonant path (from the ground state) contribute. Here, we focus on the dynamics of EWPs originating solely from the ground state, using a similar approach. As illustrated in Fig. 6(a), we employ a 4ω pulse (dark yellow) to ionize the ground-state electrons, while the atom remains dressed by the resonant field ω (red). By reconstructing the dynamics of EWPs ionized by this 4ω laser field, we can reveal the dynamics of EWPs ionized solely from the ground state. To achieve this, yet another weak 4ω pulse [colored in light yellow in Fig. 6(a)] is introduced at the

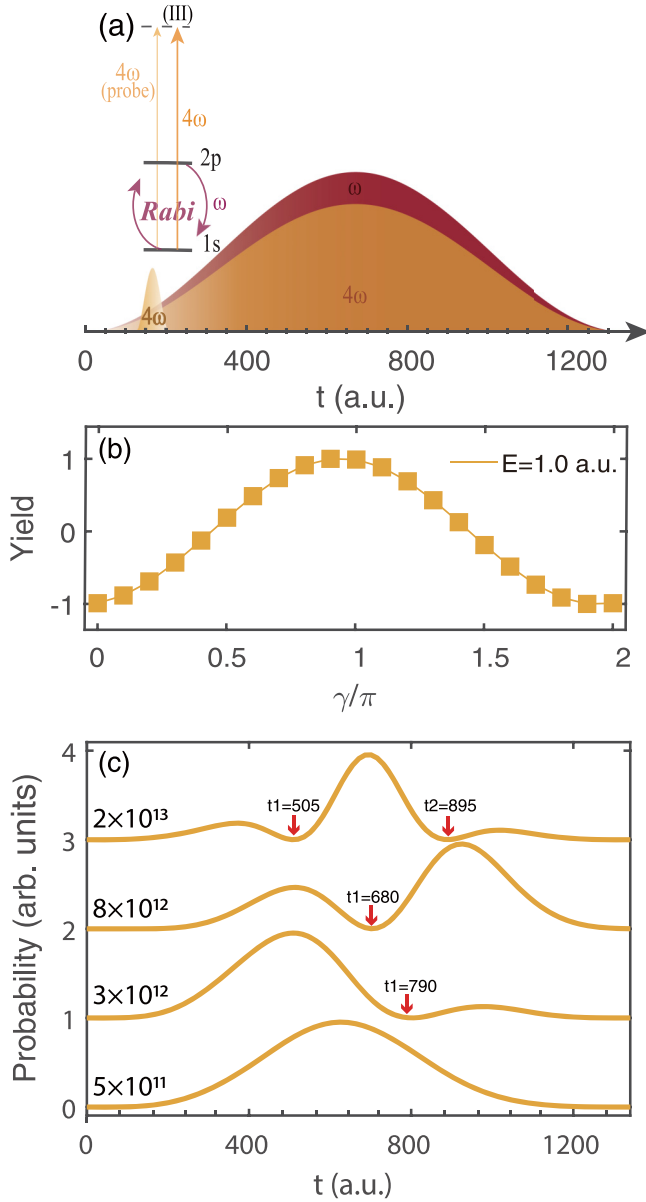


FIG. 6. (a) Schematic of the laser pulses used to probe EWP dynamics originating solely from the ground state. The 4ω pulse (dark yellow) is introduced to ionize the ground-state electron, while the ground state remains dressed by the resonant field ω (red). At the leading edge of the primary 4ω pulse (dark yellow), a weak 4ω (light yellow) laser pulse is introduced. The EWPs ionized by this weak pulse (indicated by the light yellow arrow) serve as a reference for probing the EWPs ionized by the primary 4ω pulse (indicated by the dark yellow arrow). (b) Normalized photoelectron yield as a function of the phase γ at the laser intensity of 2×10^{13} W/cm². (c) Normalized probability of the temporal profiles of EWPs $|\tilde{A}(t)|^2$ ionized solely from the Rabi-cycling ground state at laser intensities of the resonant field ω of 5×10^{11} , 3×10^{12} , 8×10^{12} , and 2×10^{13} W/cm². For visual clarity, the lines in (c) are vertically separated.

leading edge of the primary 4ω pulse, serving as the reference to probe the amplitude and phase of the ionized EWPs (see Appendix C for a detailed discussion on the role of these two 4ω pulses). The CEP of this weak 4ω pulse γ changes from

0 to 2π . The interference between the EWPs ionized by these two 4ω pulses results in the phase (γ)-dependent oscillation photoelectron yield, as shown in Fig. 6(b). By fitting the oscillating photoelectron yields at different energies within the energy range 0.98–1.02 a.u. with the cosine function, we extract the amplitudes and phases of the EWPs. Then, the ionization dynamics from the Rabi-cycling ground state can be reconstructed [i.e., the path III in Fig. 1(c)].

Figure 6(c) shows the reconstructed probability of the temporal EWPs (ionization rate) solely from the ground state (due to the 4ω laser), where the intensities of the resonant dressing field ω are 5×10^{11} , 3×10^{12} , 8×10^{12} , and

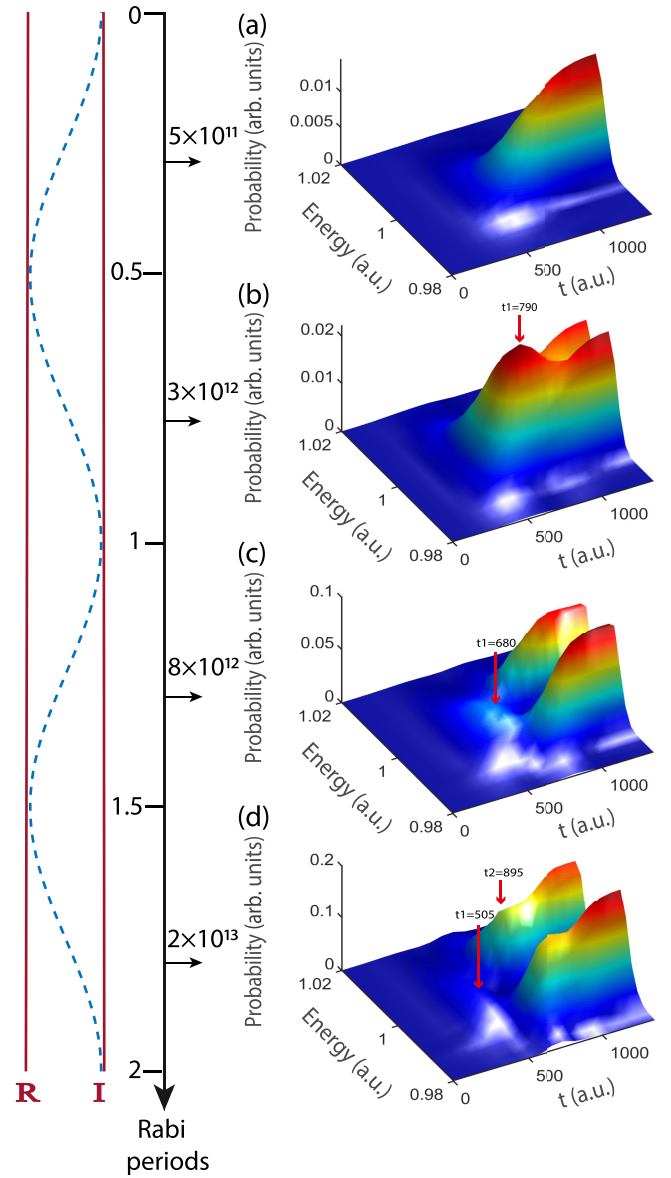


FIG. 7. Time evolution of the photoelectron energy spectrum ionized solely from the Rabi-cycling ground state at the laser intensities of the resonant field ω of (a) 5×10^{11} , (b) 3×10^{12} , (c) 8×10^{12} , and (d) 2×10^{13} W/cm². $P(E, t)$ in [(a)–(d)] is obtained through the absorption of a 4ω photon from the ground state, while the ground state remains dressed by the resonant field ω .

2×10^{13} W/cm², respectively. Compared to the results for the resonant TPI [shown in Fig. 2(c)], the probability of the temporal EWPs (ionization rate) exhibit more troughs at the same laser intensity. The troughs in the temporal EWPs approximately coincide with $1/2$ ($t_1 = 790$ a.u., 680 a.u., and 505 a.u. for the different laser intensities) and $3/2$ ($t_2 = 895$ a.u. for the highest laser intensity) Rabi periods. Using these temporal wave packets, we reconstruct the time-evolving energy spectrum through Eq. (6), as shown in Fig. 7. Compared to the resonant TPI results [shown in Figs. 3(b) to 3(i)], the decrease, and splitting of $P(E, t)$ occur at lower laser intensities. The times required to reach the extrema (as indicated by the arrows) also approximately coincide with $1/2$ and $3/2$ Rabi periods. These distinct differences arise from the evolution of EWPs solely contributed by the nonresonant path, which are controlled by the oscillatory amplitude of the ground state $\tilde{a}_I(t)$, rather than that of the resonant state $\tilde{a}_R(t)$ in the resonant TPI. The signs of $\tilde{a}_I(t)$ [$\sim \cos(\frac{1}{2}\Omega t)$] flip at each half-integer Rabi period. Consequently, the extrema in the temporal EWPs and time-evolving energy spectrum are synchronized with half-integer multiples of the Rabi period. Moreover, the complete splitting of the spectrum occurs at integer multiples of the Rabi period, which happens twice within the first two Rabi periods, as shown in Fig. 1(b) (indicated by the two red arrows).

At the more intense laser intensity, the nonresonant path from the ground state may dominate the resonant TPI, rather than the resonant path [34,46]. The spectrum splitting is expected to occur at integer multiples of the Rabi period, rather than at even numbers of the Rabi period in the resonant path. For different partial waves, this transformation may occur at different laser intensities owing to the different contributions of the nonresonant path.

IV. CONCLUSION

We investigated the resonant TPI process during the buildup of Rabi oscillations. By employing spectrally and angularly resolved electron interferometry, we separately retrieved the phases of the s and d partial waves and revealed the electron dynamics in this nonperturbative ionization process. Our results showed that the temporal evolutions of the s and d waves overall were the same, such as the oscillations in the temporal profile of the EWPs. With the three-level model, we demonstrated that, in the resonant path, the temporal profiles should be the same for the s and d waves. When the nonresonant path contributes, the temporal profiles of these two partial waves are different. Thus, the minor difference between the s and d waves in the temporal EWPs indicates the different

contributions from the nonresonant path. Furthermore, the three-level model revealed the difference in the asymmetry of the energy spectra for the resonant and nonresonant paths. This difference results from the opposite impact of the AC-Stark effect on the resonant and nonresonant paths. When the contributions from the resonant and nonresonant paths are coherently summed, the s and d partial waves show different asymmetric behaviors. The probability at the lower-energy peak of the AT doublets is higher for the d wave, while lower for the s wave.

Our work revealed the influence of the oscillating populations on the dynamics of resonant and nonresonant paths. Furthermore, we provided a way for quantitatively assessing the partial-wave resolved contribution of the nonresonant path in the time domain. The procedure demonstrated in our work can be extended to study other intricate processes in the Rabi-cycling system, such as dynamic interference [50,64] and stabilization against photoionization [46]. Additionally, the electron interferometry with two phase-locked XUV pulses is experimentally accessible in free-electron laser facilities [14,15], thus attracting experimental interest to our findings.

ACKNOWLEDGMENTS

This work was supported by National Key Research and Development Program of China (Grant No. 2019YFA0308300), National Natural Science Foundation of China (Grants No. 12374264 and No. 12204545). The computing work in this paper is supported by the Public Service Platform of High Performance Computing provided by Network and Computing Center of Huazhong University of Science and Technology (HUST).

APPENDIX: THREE-LEVEL MODEL AND SCHEMATIC ILLUSTRATION OF IONIZATION PATHS

1. Three-level model

In the resonant TPI process, the time-dependent wave function can be expanded as

$$|\Psi\rangle = a_I(t)e^{-iE_I t}|I\rangle + a_R(t)e^{-iE_R t}|R\rangle + \sum_n \int d\varepsilon a_\varepsilon(t)e^{-iE_\varepsilon t}|\varepsilon\rangle, \quad (\text{A1})$$

where $|I\rangle$ and $|R\rangle$ represent the ground and the resonant states, respectively. $|\varepsilon\rangle$ represents the continuum states, and all the nonresonant states are labeled by $|n\rangle$. Thus, the minimal three-level model to calculate the results of the resonant TPI is obtained as [45]

$$i\dot{a}_I(t) = \left[S_I(t) - \frac{i}{2}\Gamma_I(t) \right] a_I(t) + D_{IR} \frac{1}{2} E_0 g(t) e^{i\Delta\omega t} a_R(t), \quad (\text{I})$$

$$i\dot{a}_R(t) = D_{IR} \frac{1}{2} E_0 g(t) e^{-i\Delta\omega t} a_I(t) + \left[S_R(t) - \frac{i}{2}\Gamma_R(t) \right] a_R(t), \quad (\text{II})$$

$$i\dot{a}_\varepsilon(t) = \tilde{M}_{I\varepsilon}^\dagger \left(\frac{1}{2} E_0 g(t) \right)^2 e^{-i\delta t} a_I(t) + D_{Re} \frac{1}{2} E_0 g(t) e^{-i\delta t} a_R(t) + S_\varepsilon(t) a_\varepsilon(t) \quad (\text{III}). \quad (\text{A2})$$

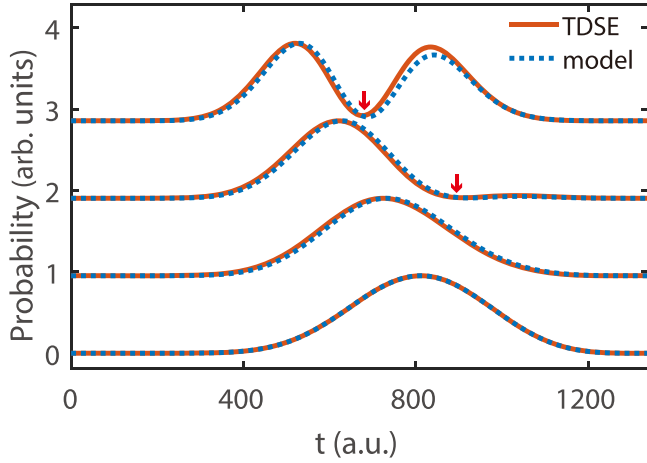


FIG. 8. Normalized probability of the total ($s + d$) temporal profiles of EWPs $|\tilde{A}_s(t) + \tilde{A}_d(t)|^2$ from TDSE (solid orange lines) and from the three-level model (dashed blue lines) at laser intensities of 5×10^{11} , 3×10^{12} , 8×10^{12} , and 2×10^{13} W/cm².

Here, $\Delta\omega = \omega - \omega_{RI}$ ($\omega_{ij} = E_i - E_j$) is the energy detuning, $D_{IR} = \langle I|\hat{z}|R\rangle$, $D_{R\varepsilon} = \langle R|\hat{z}|\varepsilon\rangle$ are defined as the transition dipole matrix element between the ground and resonant states, the resonant and continuum states, respectively.

$$\begin{aligned} \delta &= E_R - E_\varepsilon + \omega, \\ \delta_I &= E_I - E_\varepsilon + 2\omega \end{aligned} \quad (\text{A3a})$$

are the energy detunings,

$$\tilde{M}_{I\varepsilon} = \sum_{n \neq I, \neq R} \frac{\langle I|z|n\rangle \langle n|z|\varepsilon\rangle}{E_\varepsilon - E_n - \omega + i\Gamma} \quad (\text{A3b})$$

is the two-photon transition matrix element from the ground state to the continuum state through the non-resonant states

$$\begin{aligned} S_\varepsilon(t) &= U_p(t), \\ S_I(t) &= \sum_{n \neq I, \neq R} \left(D_{In} \frac{1}{2} E_0 g(t) \right)^2 \frac{2\omega_{In}}{\omega_{In}^2 - \omega^2} = S_{I0} E_0^2 g^2(t), \\ S_R(t) &= \sum_{n \neq I, \neq R} \left(D_{Rn} \frac{1}{2} E_0 g(t) \right)^2 \frac{2\omega_{Rn}}{\omega_{Rn}^2 - \omega^2} = S_{R0} E_0^2 g^2(t) \end{aligned} \quad (\text{A3c})$$

are the dynamic stark shifts of the continuum, ground and resonant states, respectively. The stark shift for the continuum state approximately equals to the time-dependent ponderomotive shift $U_p(t) = \frac{E_0^2}{4\omega^2} g^2(t)$,

$$\begin{aligned} \Gamma_R(t) &= 2\pi |D_{R\varepsilon}|^2 \left(\frac{1}{2} E_0 g(t) \right)^2, \\ \Gamma_I(t) &= 2\pi |\tilde{M}_{I\varepsilon}|^2 \left(\frac{1}{2} E_0 g(t) \right)^4, \end{aligned} \quad (\text{A3d})$$

represent the ionization rates from the resonant state $|R\rangle$ and the ground state $|I\rangle$, respectively.

For clarity, we further redefine the amplitudes a_I , a_R and a_ε in Eq. (A2) as $\tilde{a}_I e^{-iS_I(t)}$, $-i\tilde{a}_R e^{-iS_R(t)}$ and $\tilde{a}_\varepsilon e^{-iS_\varepsilon(t)}$ [44,45]. Additionally, we redefine $D_{R\varepsilon}$ as $i\tilde{D}_{R\varepsilon}$ to maintain consistency with $\tilde{M}_{I\varepsilon}$ ($\tilde{M}_{I\varepsilon}$ is a complex value). The terms $-i\Gamma_I$ and $-i\Gamma_R$

are neglected due to they are small terms. Then, the time-dependent expression for the continuum state simplifies to

$$\begin{aligned} i\dot{\tilde{a}}_\varepsilon(t) &= \tilde{M}_{I\varepsilon}^\dagger \left(\frac{1}{2} E_0 g(t) \right)^2 e^{-i\tilde{\delta}_I t} \tilde{a}_I(t) \\ &+ \tilde{D}_{R\varepsilon}^\dagger \frac{1}{2} E_0 g(t) e^{-i\tilde{\delta}_I t} \tilde{a}_R(t). \end{aligned} \quad (\text{A4})$$

The terms $\tilde{\delta} = E_R + S_R - E_\varepsilon - S_\varepsilon + \omega$ and $\tilde{\delta}_I = E_I + S_I - E_\varepsilon - S_\varepsilon + 2\omega$ represent the energy detunings between the shifted energy levels. The $\tilde{a}_I(t)$ and $\tilde{a}_R(t)$ represent the oscillating amplitudes of the ground and the resonant states

$$\begin{aligned} \tilde{a}_I(t) &= \left[\cos \frac{\Omega t}{2} - i \frac{\Delta\omega}{\Omega} \sin \frac{\Omega t}{2} \right] \exp \left(\frac{i\Delta\omega t}{2} \right) \\ \tilde{a}_R(t) &= \frac{E_0 D_{IR}}{\Omega} \sin \frac{\Omega t}{2} \exp \left(\frac{-i\Delta\omega t}{2} \right), \end{aligned} \quad (\text{A5})$$

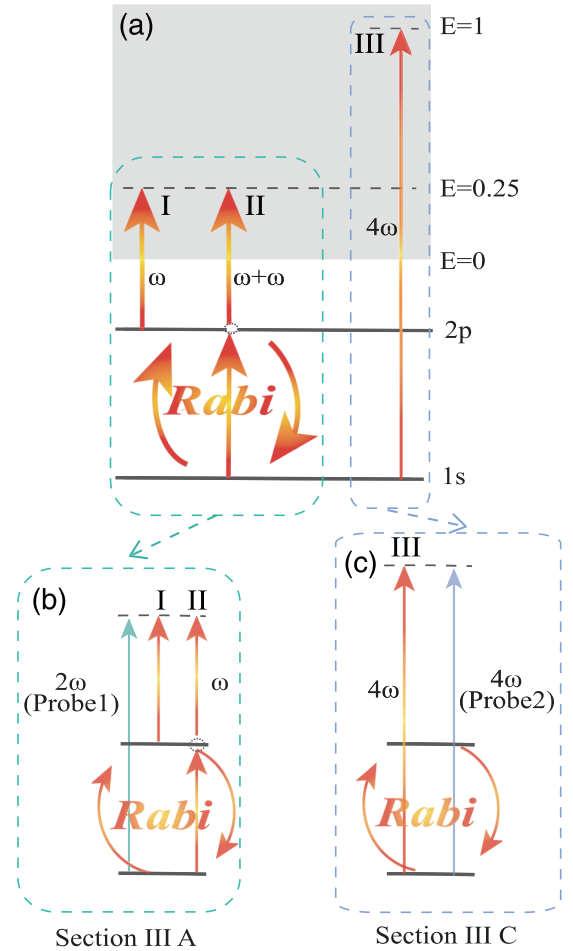


FIG. 9. (a) Schematic diagrams of the ionization paths studied in our work. Paths I and II represent the resonant and nonresonant ionization paths, respectively, in the TPI process. Path III represents the ionization path solely from the Rabi-cycling ground state. (b) Schematic illustrating the electron interferometry for reconstructing the continuum EWP dynamic in the resonant TPI (i.e., EWPs from paths I and II). The detailed reconstruction process is elaborated in Sec. III A. (c) Schematic illustrating the electron interferometry for reconstructing the continuum EWP dynamics solely from the Rabi-cycling ground state (i.e., EWPs from path III). The detailed reconstruction process is elaborated in Sec. III C.

where the term Ω denotes the effective Rabi frequency. The energy detuning $\Delta\omega$ is 0 in our work, and the Stark shifts are small within the intensity range considered; thus, $\tilde{a}_I(t)$ and $\tilde{a}_R(t)$ can be approximately written as $\tilde{a}_I(t) \approx \cos \frac{\Omega t}{2}$ and $\tilde{a}_R(t) \approx \sin \frac{\Omega t}{2}$.

2. Results of the three-level model

Figure 8 displays (the probability of) the temporal profiles of EWPs for the sum of the s and d waves from both the three-level model and the TDSE. The results calculated from the three-level model are in good agreement with those reconstructed from the TDSE data. This agreement confirms that the reconstructed temporal EWPs from the TDSE data, as depicted in Fig. 2, indeed correspond to the equation derived from the three-level model [Eq. (8)], thereby validating the analysis presented in Sec. III B.

3. Schematic diagram of all ionization paths

Figure 9(a) illustrates the three ionization paths investigated in our study during the build up of Rabi oscillations. Paths I and II represent the resonant (originating from the resonant state) and nonresonant ionization (from the ground state) paths, respectively, involved in the resonant two-photon

ionization process [34,45]. Since the photoelectrons ionized from the ground state via path II mix with those from the resonant state via path I at the energy $E = 0.25$ a.u., and path II is significantly weaker than path I [34,45], observing the photoelectron dynamics from the ground-state via path II is challenging. Therefore, we introduce a higher frequency laser field (4ω field) to ionize the electron in the Rabi-cycling ground state to a higher energy $E = 1.0$ a.u. (path III). Photoelectrons from the ground state via path III no longer mix with those from the resonant state. Through this method, the dynamics of the ground state, and thus the nonresonant ionization path, can be isolated and revealed.

To further reveal the buildup of Rabi oscillations in real time, electron interferometry is utilized to reconstruct the continuum EWP dynamics in the resonant TPI (i.e., EWPs from paths I and II), as well as those solely from the Rabi-cycling ground state (i.e., EWPs from path III), as shown in Figs. 9(b) and 9(c), respectively. Figure 9(b) shows that a 2ω pulse (Probe1) is introduced to probe the amplitudes and the phases of the EWPs from paths I and II. The detailed reconstruction process is elaborated in Sec. III A. Similarly, a (weak) 4ω pulse (Probe2) is introduced to probe the amplitudes and phases of the EWPs from Path III, as illustrated in Fig. 9(c). The detailed reconstruction process is presented in Sec. III C.

-
- [1] R. Kienberger, E. Goulielmakis, M. Uiberacker, A. Baltuska, V. Yakovlev, F. Bammer, A. Scrinzi, T. Westerwalbesloh, U. Kleineberg, U. Heinzmann, M. Drescher, and F. Krausz, Atomic transient recorder, *Nature (London)* **427**, 817 (2004).
- [2] J. Su, H. Ni, A. Jaroń-Becker, and A. Becker, Time delays in two-photon ionization, *Phys. Rev. Lett.* **113**, 263002 (2014).
- [3] Z. Guo, P. Ge, Y. Fang, Y. Dou, X. Yu, J. Wang, Q. Gong, and Y. Liu, Probing molecular frame wigner time delay and electron wavepacket phase structure of CO molecule, *Ultrafast Science* **2022**, 9802917 (2022).
- [4] M. Swoboda, T. Fordell, K. Klünder, J. M. Dahlström, M. Miranda, C. Buth, K. J. Schafer, J. Mauritsson, A. L'Huillier, and M. Gisselbrecht, Phase measurement of resonant two-photon ionization in helium, *Phys. Rev. Lett.* **104**, 103003 (2010).
- [5] A. S. Kheifets, Strongly resonant reconstruction of attosecond beating by interference of two-photon transitions on lithium, *Phys. Rev. A* **104**, L021103 (2021).
- [6] A. S. Kheifets and A. W. Bray, Rabbitt phase transition across the ionization threshold, *Phys. Rev. A* **103**, L011101 (2021).
- [7] X. Yu, M. Han, Z. Guo, and Y. Liu, Intrinsic resonant photoionization time delay of hydrogen atoms probed with attosecond beating of asymmetrical photon transitions, *Phys. Rev. A* **104**, 063108 (2021).
- [8] L. Neoričić, D. Busto, H. Laurell, R. Weissenbilder, M. Ammitzböll, S. Luo, J. Peschel, H. Wikmark Kreuger, J. Lahl, S. Maclot, R. Squibb, S. Zhong, P. Eng-Johnsson, C. Arnold, R. Feifel, M. Gisselbrecht, E. Lindroth, and A. L'Huillier, Resonant two-photon ionization of helium atoms studied by attosecond interferometry, *Front. Phys.* **10**, 964586 (2022).
- [9] A. Autuori, D. Platzer, M. Lejman, G. Gallician, L. Maëder, A. Covolo, L. Bosse, M. Dalui, D. Bresteau, J.-F. Hergott, O. Tcherbakoff, H. Marroux, V. Loriot, F. Lépine, L. Poisson, R. Taieb, J. Caillat, and P. Salieres, Anisotropic dynamics of two-photon ionization: An attosecond movie of photoemission, *Sci. Adv.* **8**, eabl7594 (2022).
- [10] L. Drescher, T. Witting, O. Kornilov, and M. J. J. Vrakking, Phase dependence of resonant and antiresonant two-photon excitations, *Phys. Rev. A* **105**, L011101 (2022).
- [11] Y. Liao, Y. Zhou, L.-W. Pi, J. Liang, Q. Ke, Y. Zhao, M. Li, and P. Lu, Reconstruction of attosecond beating by interference of two-photon transitions on the lithium atom with Rabi oscillations, *Phys. Rev. A* **105**, 063110 (2022).
- [12] P.-M. Paul, E. Toma, P. Breger, G. Mullot, F. Audebert, P. Balcou, H. Muller, and P. Agostini, Observation of a train of attosecond pulses from high harmonic generation, *Science* **292**, 1689 (2001).
- [13] J. Liang, M. Han, Y. Liao, J.-B. Ji, C. Leung, W.-C. Jiang, K. Ueda, Y. Zhou, P. Lu, and H. J. Wörner, Attosecond-resolved non-dipole photoionization dynamics, *Nat. Photonics* **18**, 311 (2024).
- [14] M. Di Fraia, O. Plekan, C. Callegari, K. C. Prince, L. Giannessi, E. Allaria, L. Badano, G. De Ninno, M. Trovò, B. Diviacco *et al.*, Complete characterization of phase and amplitude of bichromatic extreme ultraviolet light, *Phys. Rev. Lett.* **123**, 213904 (2019).
- [15] D. You, K. Ueda, E. V. Gryzlova, A. N. Grum-Grzhimailo, M. M. Popova, E. I. Staroselskaya, O. Tugs, Y. Orimo, T. Sato, K. L. Ishikawa *et al.*, New method for measuring angle-resolved phases in photoemission, *Phys. Rev. X* **10**, 031070 (2020).
- [16] A. N. Grum-Grzhimailo, E. V. Gryzlova, E. I. Staroselskaya, J. Venzke, and K. Bartschat, Interfering one-photon and two-photon ionization by femtosecond VUV pulses in the region of an intermediate resonance, *Phys. Rev. A* **91**, 063418 (2015).

- [17] N. Douguet, A. N. Grum-Grzhimailo, E. V. Gryzlova, E. I. Staroselskaya, J. Venzke, and K. Bartschat, Photoelectron angular distributions in bichromatic atomic ionization induced by circularly polarized VUV femtosecond pulses, *Phys. Rev. A* **93**, 033402 (2016).
- [18] N. Douguet, E. Gryzlova, E. Staroselskaya, K. Bartschat, and A. Grum-Grzhimailo, Photoelectron angular distribution in two-pathway ionization of neon with femtosecond XUV pulses, *Eur. Phys. J. D* **71**, 105 (2017).
- [19] E. V. Gryzlova, A. N. Grum-Grzhimailo, E. I. Staroselskaya, N. Douguet, and K. Bartschat, Quantum coherent control of the photoelectron angular distribution in bichromatic-field ionization of atomic neon, *Phys. Rev. A* **97**, 013420 (2018).
- [20] E. V. Gryzlova, P. Carpeggiani, M. M. Popova, M. D. Kiselev, N. Douguet, M. Reduzzi, M. Negro, A. Comby, H. Ahmadi, V. Wanie *et al.*, Influence of an atomic resonance on the coherent control of the photoionization process, *Phys. Rev. Res.* **4**, 033231 (2022).
- [21] J. Peschel, D. Busto, M. Plach, M. Bertolino, M. Hoflund, S. Maclot, J. Vinbladh, H. Wikmark Kreuger, F. Zapata, E. Lindroth, M. Gisselbrecht, J. Dahlström, A. L'Huillier, and P. Eng-Johnsson, Attosecond dynamics of multi-channel single photon ionization, *Nat. Commun.* **13**, 5205 (2022).
- [22] S. Beaulieu, A. Comby, A. Clergerie, J. Caillat, D. Descamps, N. Dudovich, B. Fabre, R. Géneaux, F. Légaré, S. Petit, B. Pons, G. Porat, T. Ruchon, R. Taïeb, V. Blanchet, and Y. Mairesse, Attosecond-resolved photoionization of chiral molecules, *Science* **358**, 1288 (2017).
- [23] M. Zitnik, A. Mihelic, K. Bucar, S. Krusic, R. Squibb, R. Feifel, I. Ismail, P. Lablanquie, J. Palaudox, O. Plekan, M. Di Fraia, M. Coreno, M. Manfredda, A. Simoncig, P. Ribic, F. Sottocorona, E. Allaria, K. Prince, C. Callegari, and F. Penent, Interference of two-photon transitions induced by XUV light, *Optica* **9**, 692 (2022).
- [24] R. Y. Bello, V. J. Borràs, J. Gonzalez-Vazquez, and F. Martín, Electronic coherences in argon through interfering one- and two-photon ionization processes in the vicinity of feshbach resonances, *Phys. Rev. Res.* **4**, 043028 (2022).
- [25] M. Kotur, D. Guenot, Á. Jiménez-Galán, D. Kroon, E. Larsen, M. Louisy, S. Bengtsson, M. Miranda, J. Mauritsson, C. Arnold, S. Canton, M. Gisselbrecht, T. Carette, J. Dahlström, E. Lindroth, A. Maquet, L. Argenti, F. Martín, and A. L'Huillier, Spectral phase measurement of a fano resonance using tunable attosecond pulses, *Nat. Commun.* **7**, 10566 (2016).
- [26] V. Gruson, L. Barreau, A. Jimenez-Galan, F. Risoud, J. Caillat, A. Maquet, B. Carre, F. Lepetit, J.-F. Hergott, T. Ruchon, L. Argenti, R. Taïeb, F. Martín, and P. Salieres, Attosecond dynamics through a fano resonance: Monitoring the birth of a photoelectron, *Science* **354**, 734 (2016).
- [27] D. Busto, L. Barreau, M. Isinger, M. Turconi, C. Alexandridi, A. Harth, S. Zhong, R. Squibb, D. Kroon, S. Plogmaker, M. Miranda, Á. Jiménez-Galán, L. Argenti, C. Arnold, R. Feifel, F. Martín, M. Gisselbrecht, A. L'Huillier, and P. Salieres, Time-frequency representation of autoionization dynamics in helium, *J. Phys. B: At., Mol. Opt. Phys.* **51**, 044002 (2018).
- [28] S. H. Autler and C. H. Townes, Stark effect in rapidly varying fields, *Phys. Rev.* **100**, 703 (1955).
- [29] B. Walker, M. Kaluža, B. Sheehy, P. Agostini, and L. F. DiMauro, Observation of continuum-continuum Autler-Townes splitting, *Phys. Rev. Lett.* **75**, 633 (1995).
- [30] J. Qi, G. Lazarov, X. Wang, L. Li, L. M. Narducci, A. M. Lyyra, and F. C. Spano, Autler-Townes splitting in molecular lithium: Prospects for all-optical alignment of nonpolar molecules, *Phys. Rev. Lett.* **83**, 288 (1999).
- [31] E. H. Ahmed, S. Ingram, T. Kirova, O. Salihoglu, J. Huennekens, J. Qi, Y. Guan, and A. M. Lyyra, Quantum control of the spin-orbit interaction using the Autler-Townes effect, *Phys. Rev. Lett.* **107**, 163601 (2011).
- [32] M. G. Bustamante, V. D. Rodríguez, and R. O. Barrachina, Secondary peaks in the atomic ionization by a resonant laser pulse, *J. Phys.: Conf. Ser.* **397**, 012014 (2012).
- [33] W.-C. Jiang, H. Liang, S. Wang, L.-Y. Peng, and J. Burgdörfer, Enhancing Autler-Townes splittings by ultrafast XUV pulses, *Phys. Rev. Res.* **3**, L032052 (2021).
- [34] S. Nandi, E. Olofsson, M. Bertolino, S. Carlström, F. Zapata, D. Busto, C. Callegari, M. Di Fraia, P. Eng-Johnsson, R. Feifel *et al.*, Observation of Rabi dynamics with a short-wavelength free-electron laser, *Nature (London)* **608**, 488 (2022).
- [35] E. P. Kanter, B. Krässig, Y. Li, A. M. March, P. Ho, N. Rohringer, R. Santra, S. H. Southworth, L. F. DiMauro, G. Doumy, C. A. Roedig, N. Berrah, L. Fang, M. Hoener, P. H. Bucksbaum, S. Ghimire, D. A. Reis, J. D. Bozek, C. Bostedt, M. Messerschmidt, and L. Young, Unveiling and driving hidden resonances with high-fluence, high-intensity x-ray pulses, *Phys. Rev. Lett.* **107**, 233001 (2011).
- [36] T. Sako, J. Adachi, A. Yagishita, M. Yabashi, T. Tanaka, M. Nagasono, and T. Ishikawa, Suppression of ionization probability due to Rabi oscillations in the resonance two-photon ionization of He by EUV free-electron lasers, *Phys. Rev. A* **84**, 053419 (2011).
- [37] P. V. Demekhin and L. S. Cederbaum, Strong interference effects in the resonant auger decay of atoms induced by intense x-ray fields, *Phys. Rev. A* **83**, 023422 (2011).
- [38] T. Sato, A. Iwasaki, K. Ishibashi, T. Okino, K. Yamanouchi, J. Adachi, A. Yagishita, H. Yazawa, F. Kannari, M. Aoyama, K. Yamakawa, K. Midorikawa, H. Nakano, M. Yabashi, M. Nagasono, A. Higashiya, and T. Ishikawa, Determination of the absolute two-photon ionization cross section of He by an XUV free electron laser, *J. Phys. B: At., Mol. Opt. Phys.* **44**, 161001 (2011).
- [39] N. Miyauchi, J.-I. Adachi, A. Yagishita, T. Sako, F. Koike, T. Sato, A. Iwasaki, T. Okino, K. Yamanouchi, K. Midorikawa, K. Yamakawa, F. Kannari, H. Nakano, M. Nagasono, K. Tono, M. Yabashi, T. Ishikawa, T. Togashi, H. Ohashi, and Y. Senba, Three-photon double ionization of Ar studied by photoelectron spectroscopy using an extreme ultraviolet free-electron laser: Manifestation of resonance states of an intermediate Ar⁺ ion, *J. Phys. B: At. Mol. Opt. Phys.* **44**, 071001 (2011).
- [40] B. Kaiser, A. Brand, M. Glässl, A. Vagov, V. M. Axt, and U. Pietsch, Photoionization of resonantly driven atomic states by an extreme ultraviolet-free-electron laser: intensity dependence and renormalization of Rabi frequencies, *New J. Phys.* **15**, 093016 (2013).
- [41] M. Fushitani, C. Liu, A. Matsuda, T. Endo, Y. Toida, M. Nagasono, T. Togashi, M. Yabashi, T. Ishikawa, Y. Hikosaka, T. Morishita, and A. Hishikawa, Femtosecond two-photon Rabi

- oscillations in excited he driven by ultrashort intense laser fields, *Nat. Photonics* **10**, 102 (2015).
- [42] D. A. Tumakov, D. A. Telnov, G. Plunien, and V. M. Shabaev, Photoelectron spectra after multiphoton ionization of Li atoms in the one-photon Rabi-flopping regime, *Phys. Rev. A* **100**, 023407 (2019).
- [43] W. Li, Y. Lei, X. Li, T. Yang, M. Du, Y. Jiang, J. Li, A. Liu, L. He, P. Ma *et al.*, New source for tuning the effective Rabi frequency discovered in multiphoton ionization, [arXiv:2112.13096](https://arxiv.org/abs/2112.13096).
- [44] A. Tóth and A. Csehi, Probing strong-field two-photon transitions through dynamic interference, *J. Phys. B: At., Mol. Opt. Phys.* **54**, 035005 (2021).
- [45] X. Zhang, Y. Zhou, Y. Liao, Y. Chen, J. Liang, Q. Ke, M. Li, A. Csehi, and P. Lu, Effect of nonresonant states in near-resonant two-photon ionization of hydrogen, *Phys. Rev. A* **106**, 063114 (2022).
- [46] E. Olofsson and J. M. Dahlström, Photoelectron signature of dressed-atom stabilization in an intense XUV field, *Phys. Rev. Res.* **5**, 043017 (2023).
- [47] A. Tóth, S. Borbély, Y. Zhou, and A. Csehi, Role of dynamic stark shifts in strong-field excitation and subsequent ionization, *Phys. Rev. A* **107**, 053101 (2023).
- [48] N. Simonović, D. Popović, and A. Bunjac, Manifestations of Rabi dynamics in the photoelectron energy spectra at resonant two-photon ionization of atom by intense short laser pulses, *Atoms* **11**, 20 (2023).
- [49] Y.-J. Mao, H.-B. Yao, M. He, Z.-H. Zhang, Y. Li, and F. He, Unveiling Rabi dynamics through angle-resolved photoelectron momentum distributions using an ω - 2ω pulse pair, *Phys. Rev. A* **108**, 053117 (2023).
- [50] A. Toth, S. Borbély, and A. Csehi, Dynamic interference in below-threshold ionization, *Phys. Rev. A* **108**, L061101 (2023).
- [51] A. Desrier, A. Maquet, R. Taieb, and J. Caillat, Ionization dynamics through a fano resonance: Time-domain interpretation of spectral amplitudes, *Phys. Rev. A* **98**, 053406 (2018).
- [52] Z. Zhao and C. D. Lin, Theory of laser-assisted autoionization by attosecond light pulses, *Phys. Rev. A* **71**, 060702(R) (2005).
- [53] M. Wickenhauser, J. Burgdörfer, F. Krausz, and M. Drescher, Time resolved fano resonances, *Phys. Rev. Lett.* **94**, 023002 (2005).
- [54] T. Mercouris, Y. Komninos, and C. A. Nicolaides, Time-dependent formation of the profile of the he $2s2p^1P^o$ state excited by a short laser pulse, *Phys. Rev. A* **75**, 013407 (2007).
- [55] A. Kaldun, A. Blättermann, V. Stoß, S. Donsa, H. Wei, R. Pazourek, S. Nagele, C. Ott, C. D. Lin, J. Burgdorfer, and T. Pfeifer, Observing the ultrafast buildup of a fano resonance in the time domain, *Science* **354**, 738 (2016).
- [56] M. Han, H. Liang, J. bao Ji, L. C. Sum, K. Ueda, J. M. Rost, and H. J. Wörner, Laser-assisted fano resonance: Attosecond quantum control and dynamical imaging, [arXiv:2302.04090v1](https://arxiv.org/abs/2302.04090v1).
- [57] C. Ott, A. Kaldun, P. Raith, K. Meyer, M. Laux, J. Evers, C. Keitel, C. Greene, and T. Pfeifer, Lorentz meets fano in spectral line shapes: A universal phase and its laser control, *Science* **340**, 716 (2013).
- [58] W.-C. Chu and C. D. Lin, Theory of ultrafast autoionization dynamics of fano resonances, *Phys. Rev. A* **82**, 053415 (2010).
- [59] J. Liang, Y. Zhou, Y. Liao, W.-C. Jiang, M. Li, and P. Lu, Direct visualization of deforming atomic wavefunction in ultraintense high-frequency laser pulses, *Ultrafast Science* **2022**, 9842716 (2022).
- [60] T. N. Rescigno and C. W. McCurdy, Numerical grid methods for quantum-mechanical scattering problems, *Phys. Rev. A* **62**, 032706 (2000).
- [61] W.-C. Jiang and X. Tian, Efficient split-lanczos propagator for strong-field ionization of atoms, *Opt. Express* **25**, 26832 (2017).
- [62] D. G. Arbó, J. E. Miraglia, M. S. Gravielle, K. Schiessl, E. Persson, and J. Burgdörfer, Coulomb-volkov approximation for near-threshold ionization by short laser pulses, *Phys. Rev. A* **77**, 013401 (2008).
- [63] T. Pfeifer, Y. Jiang, S. Düsterer, R. Moshhammer, and J. Ullrich, Partial-coherence method to model experimental free-electron laser pulse statistics, *Opt. Lett.* **35**, 3441 (2010).
- [64] P. V. Demekhin and L. S. Cederbaum, Coherent intense resonant laser pulses lead to interference in the time domain seen in the spectrum of the emitted particles, *Phys. Rev. A* **86**, 063412 (2012).